Materials Today Sustainability 30 (2025) 101106

Contents lists available at ScienceDirect

Materials Today Sustainability

journal homepage: www.journals.elsevier.com/materials-today-sustainability

Coarse-grained molecular studies reveal potential for increased CO_2 storage in hydrates

Meisam Adibifard, Olufemi Olorode *

Department of Petroleum Engineering, Louisiana State University, Baton Rouge, LA 70803, United States

ARTICLE INFO

Dataset link: https://github.com/UnconvRS/CO2HydrateMD

Keywords:
Energy storage in gas hydrate structures
Gas nanobubble trapping
Greenhouse gas storage nanomaterials
Hydrate-based clean energy storage
Molecular dynamics simulation of gas hydrate nanostructures

ABSTRACT

The interest in curtailing global warming has accelerated research in capturing and storing carbon dioxide (CO_2), which accounts for 76% of all greenhouse gases. Considering the potential of capturing, storing, and transporting CO_2 as hydrates, several researchers have performed molecular dynamics (MD) and experimental studies of the formation and dissociation of gas hydrates. Although these studies have illustrated essential mechanisms, such as the nucleation and growth of gas hydrates, we show that the small length scales of these studies limit them to processes smaller than the sizes of the domain simulated. To address this limitation, we performed MD studies of CO_2 hydrate growth in systems that are two orders of magnitude larger than in previous studies. This allowed us to observe the trapping of CO_2 nanobubbles within a growing solid hydrate for the first time. We computed the CO_2 density in the trapped nanobubble and observed that it was 2.5 times its corresponding density in the solid hydrate, which indicates the potential to significantly increase the storage of CO_2 (and other gases) in gas hydrates. The CO_2 nanobubbles were bigger than the simulation domains used in most previous MD simulations of CO_2 hydrates, indicating the importance of these large-scale studies.

1. Introduction

Gas hydrates are icelike crystalline solids that contain gas molecules caged within the ringed frameworks formed by hydrogen bonds in water molecules. They are formed when water and certain gases co-exist at high pressures and low temperatures. They vary in structure depending on the pressure, temperature, and size of the gas molecule [1]. The three most common hydrate structures are s_I, s_{II}, and s_H structures. Of these three, CO_2 mostly forms the s_I hydrate structure in nature. Although only eight CO_2 molecules are trapped within each unit s_I hydrate structure, these hydrates have drawn considerable interest from several researchers because of their massive gas storage potential [2]. Like methane hydrates, each m^3 of a CO_2 hydrate can store 120–180 m^3 of CO_2 [1]. So, in addition to the obvious economic potential of commercially producing methane with or without injecting CO_2 into geological formations or marine sediments containing natural gas hydrates [3], several publications [4,5] have discussed the potential of CO_2 sequestration in these hydrates.

There is a consensus on the considerable change in global climate based on the interpretation of surface and satellite data and global earth models from several independent research groups [6]. Of the different changes in the global climate, the change in the average temperature is one of the most robust observations that appear to be strongly linked with the anthropogenic emission of greenhouses from the combustion of fossil fuels [7]. The observed steady increase in the average temperature of each decade since 1960 and its effects (such as the rising sea levels, more severe weather, floods, and the melting of the world's ice sheets and permafrost) has triggered global attention over the last decade. So, several researchers have proposed different technologies that focus on the capture, utilization, and underground storage of large volumes of carbon dioxide (CO_2), which accounts for approximately 76% of the total greenhouse gas emissions [8].

One of the most common targets for the underground storage of large volumes of CO_2 is in deep geological formations with sealing cap rocks, which curtail the upward migration of the CO_2 plume. Other trapping mechanisms that keep the injected CO_2 within the subsurface include its dissolution in water and chemical reactions with certain minerals in the rock to form other stable minerals. Of these different trapping mechanisms, the most reliable one for the permanent sequestration of CO_2 in the subsurface is the chemical mineralization of the injected CO_2 [9]. However, it is a prolonged process that typically occurs over hundreds or thousands of years. So, several researchers have raised the concern of CO_2 potentially migrating more quickly to the surface (through faults, fractures, and joints, which are prevalent in subsurface rocks) based on 3D seismic data [10,11]. To address this concern, a few researchers [12,13] have proposed the idea of

---

* Corresponding author.
E-mail addresses: madibi1@lsu.edu (M. Adibifard), folorode@lsu.edu (O. Olorode).

https://doi.org/10.1016/j.mtsust.2025.101106
Received 20 August 2024; Received in revised form 28 February 2025; Accepted 31 March 2025

trapping CO_2 as an icelike solid formed when the rising CO_2 plume in these water-saturated rocks gets into the gas hydrate stability zone (GHSZ). These solid hydrates are capable of plugging the pore space and effectively curtailing the flow of fluids in porous media [13].

Oceans account for over 70% of the earth's surface. With 38,000 Giga tonnes of dissolved inorganic carbon, they are the largest natural carbon sinks [14]. Therefore, a few researchers [15,16] have suggested injecting CO_2 into the seawater, which is less dense than liquid CO_2 at depths over 2800 m. So, the CO_2 is expected to sink to the sea floor and form a lake of liquid CO_2. There is currently no plan to commercialize this idea because of the environmental concern that the liquid CO_2 will dissolve in the seawater (aided by ocean currents) and adversely affect the marine life and ecosystem [17–19]. Considering the safe storage of methane as hydrates in large amounts over millions of years in the permafrost and ocean sediments, some researchers have suggested the oceanic sequestration of CO_2 as solid hydrates to address the limitations of liquid CO_2 storage in oceans [20,21]. The CO_2 hydrate can be formed by injecting CO_2 into the sea at the hydrate stability zone. It could also be formed onshore before shipping to the ocean, where it is sunk to the sea floor by buoyancy [22–24].

The significant potential for storing CO_2 as hydrates in seawater, under the seafloor, in the permafrost, and in depleted gas fields [25] has resulted in the increased research interest in studying the thermodynamic stability of CO_2 hydrates. However, to develop commercially viable technologies for the large-scale formation of CO_2 hydrate, it is necessary to understand the kinetics of CO_2 hydrate formation. To this end, some researchers [3,12] have performed laboratory experiments that allow the macroscopic observation of the growth of gas hydrates. Kondori et al. [2] indicate that experimental studies of the thermodynamic stability and kinetics of CO_2 hydrate formation are often fraught with problems, inaccuracies, and complications that border on the control and monitoring of hydrate formation at the high pressures and low temperatures required to form gas hydrates. Therefore, several researchers have performed molecular dynamics (MD) simulations to obtain valuable insights on the thermodynamic stability and kinetics of CO_2 hydrate formation/dissociation to avoid these limitations [2]. Unfortunately, the problem of scale difference between experiments and MD simulations has led to gaps in our understanding of this natural multiscale problem of hydrate formation kinetics.

Various researchers have performed equilibrium MD simulations of gas hydrates to study how they form [26] and dissociate [27]. Most of these studies use all-atom models (AAM) like the TIP4P-ice [28] to account for the long-range electrostatic interactions in water. The elementary physical model 2 (EPM2) [29] or TraPPE [30] models, which are also AAM models, are typically used to model CO_2 interactions, and the Lorentz–Berthelot [31,32] mixing rule is used to account for the CO_2–water interactions. These models have been used to study the nucleation and growth mechanisms of CO_2 hydrates, [33,34] investigate in-situ methane recovery via CO_2 injection in methane hydrate reservoirs, [35,36] and the effect of hydrophilic and hydrophobic surfaces on CO_2 hydrate formation. [37,38] However, using AAMs typically limits the scale of such MD studies to the scale of nanometers and nanoseconds because there are at least five water molecules to every gas molecule in a CO_2 hydrate. Therefore, previous MD studies of CO_2 hydrates are limited to very few hydrate cages. This size limitation implies that certain physical mechanisms on scales larger than the simulation boxes used in the literature will not be observed in such studies.

Considering the prevalence of water in the universe and the necessity to model natural systems that contain large amounts of water, using AAMs is inadequate at the required length and time scales [39]. To address this limitation, several researchers have developed coarse-grained or UAMs that allow the modeling of large systems accurately and efficiently. Molinero and Moore [40] proposed the monoatomic water (mW) model, which essentially calibrates the Stillinger–Weber (SW) potential [41] to model water–water interactions. It has been used to reproduce the anomalies and structures in ice [42]. In addition to the water–water interactions, Jacobson and Molinero [43] calibrated the SW model for methane–water and methane–methane interactions and performed coarse-grained MD simulations of methane hydrate formation. Their calibration was achieved by tuning the SW model parameters to match the physical properties obtained from experiments and AAM results. They showed that the coarse-grained SW potentials are two to three orders of magnitude faster than atomistic force fields with Ewalds sums. This study uses the same mW model but a different parametrization of the coarse-grained potential for the CO_2–CO_2 and water–CO_2 interactions. So, the speedup from our coarse-grained simulation of CO_2 hydrate formation is expected to be of the same magnitude.

In addition to modeling water as a single particle instead of multiple particles that represent its constituent atoms and massless charge, the SW model facilitates the modeling of larger scales in space and time because it avoids the computationally expensive calculation of long-range electrostatic interaction between all pairs of atoms within the simulation domain. Using the SW model, we simulated a domain of 96 nm × 12 nm × 12 nm in Adibifard and Olorode [44] and observed the formation of methane gas nanobubbles in the solid hydrates during thermal dissociation. These nanobubbles appeared larger than the simulation domain used in most all-atom gas hydrate MD simulation studies. Unfortunately, no published mW model parameters exist for CO_2–CO_2 and CO_2–water interactions in the literature. So, this work involves finding the optimum SW model parameters that match experimental data in the literature. The tuned model is then used to perform coarse-grained MD studies of CO_2 hydrate growth.

CO_2 storage by weight percentage in pure sI hydrate crystal is only 29.8%, while water accounts for the remaining 70.2%. Although this work focuses on molecular or interfacial studies of CO_2 hydrate growth in the presence of CO_2 nanobubbles, its macroscopic application will involve supplying more CO_2 gas as the hydrate grows. So, the proposed nanobubble-enhanced CO_2 hydrate storage could significantly increase the application of hydrate-based CO_2 storage in CO_2 transport, storage, and capture. The rest of this paper discusses the methods employed in calibrating the SW potential, describes the large-scale simulations performed, and presents and discusses the novel results obtained from this rigorous study of CO_2 hydrate growth.

2. Materials and methods

This section discusses the general settings used in all the simulations performed in this work. Next, we introduce the SW potential used in all the coarse-grained MD simulations performed in this work. We then discuss our approach for calibrating the SW potential for CO_2–CO_2 and Water–CO_2 interactions. This section ends with a discussion of the large-scale CO_2 hydrate systems simulated and how we post-process the results from these simulations.

2.1. General simulation settings

We used periodic boundary conditions on all six boundary faces of the simulation domain. Although we focus on performing coarse-grained (CG) MD studies to enable the study of large-scale molecular mechanisms, we also performed some all-atom (AA) MD simulations to validate the CG model parameters. We used a time step of 10 fs for the CG MD simulations. For the barostat, we used an anisotropic pressure–length coupling in simulations containing solid hydrate crystals. In contrast, we used an isotropic pressure–length coupling in the simulations of liquid/gas systems. We used the Nosé–Hoover thermostat for the isothermal–isobaric (NPT) and canonical (NVT) ensembles and used the Nosé–Hoover barostat to keep the pressure constant in the NPT ensembles. The simulations used damping constant values of 1 and 10 ps for the thermostat and barostat. A cutoff distance of 1.8σ

was used, but the σ values were specified for each pairwise or non-pairwise interaction. All simulations were initialized from replications of the s_I hydrate unit-cell provided in Takeuchi et al. [45]. The next section details the CG intermolecular potential used in this work.

In the AA MD simulations, we used a time step of 1 fs and damping constant values of 0.1 and 1 ps in the Nosé–Hoover thermostat and barostat. We used the EPM2-flex model with flexible bonds and angles [46] with a cutoff radius of 1 nm for CO_2, whereas water was modeled using the TIP4P/Ice model [28]. The Large-scale Atomic/Molecular Massively Parallel Simulator (LAMMPS) [47] was used to perform all MD simulations in this work.

2.2. Stillinger–Weber potential

The CG MD simulations performed in this work used the Stillinger–Weber (SW) potential [41], which is a sum of pairwise/two-body and three-body interaction terms. Molinero and Moore [40] tuned this potential to obtain the monoatomic water (mW) model for representing water accurately and efficiently with a single particle. Mathematically, it is written as follows:

$$E = \sum_i \sum_{j>i} \Phi_2(r_{ij}) + \sum_i \sum_{j\neq i} \sum_{k>j} \Phi_3(r_{ij}, r_{ik}, \theta_{ijk}), \tag{1}$$

where the two-body and three-body interaction terms, Φ_2 and Φ_3 are given as:

$$\Phi_2(r_{ij}) = A\epsilon \left[B(\frac{\sigma}{r_{ij}})^4 - 1 \right] exp\left(\frac{\sigma}{r_{ij} - a\sigma} \right), \tag{2}$$

$$\Phi_3(r_{ij}, r_{ik}, \theta_{ijk}) = \lambda\epsilon \left[cos\theta_{ijk} - cos\theta_0 \right]^2 exp\left(\frac{\gamma\sigma}{r_{ij} - a\sigma} \right) exp\left(\frac{\gamma\sigma}{r_{ik} - a\sigma} \right). \tag{3}$$

This model mimics the hydrogen-bonding structure of water by adding a penalty term (Φ_3) that encourages the tetrahedral configuration of water. The interaction term (λ) controls the degree of this penalization. The two critical parameters of this model are the size scale (σ) and energy scale (ϵ). The distance between the ith and jth particles is r_{ij}, whereas θ_{ijk} is the angle between the $i-j$ and $i-k$ position vectors. The constants A, B, γ, a, and θ_0 are given as 7.049556277, 0.6022245584, 1.2, 1.8, and 109.5°, respectively [43].

The three-body interaction term is calculated only for the water–water interactions, whereas λ is set to zero for CO_2–CO_2 and water–CO_2 molecules. Although Jacobson and Molinero [43] calibrated the SW potential to experimental data to obtain the optimal model parameters for methane hydrate studies, there are no published SW potential parameters for CO_2 hydrate studies. So, the following section discusses our efforts to address this limitation.

2.3. SW model calibration for CO_2 hydrate simulation

The mW model was originally developed and tuned to reproduce the physicochemical properties of water. Molinero and Moore [40] provided the mW model parameters for water–water interactions as 6.189 kcal/mol, 2.3925 Å, and 23.15 for the energy scale (ϵ_{OO}), size scale (σ_{OO}), and the interaction term (λ_{OO}), respectively. The subscripts C and O represent CO_2 and water molecules, respectively. Jacobson and Molinero [43] performed coarse-grained MD simulations of methane hydrate formation by calibrating the SW model to represent methane–water and methane–methane interactions. To enable coarse-grained MD studies of CO_2 hydrate growth, we discuss our approach to calibrate the SW potential to model CO_2–CO_2 and water–CO_2 interactions in the following two subsections.

2.3.1. Approach to calibrate the SW model for CO_2–CO_2 interactions

Considering that only water–water interactions are modeled as three-body interactions, the three-body interaction term is set to zero for CO_2–CO_2 interactions ($\lambda_c = 0$). As in Jacobson and Molinero [43], other pairwise CO_2–CO_2 interaction parameters (A and B) were left unmodified. To find the optimal values for ϵ_{cc} and σ_{cc}, we used Latin Hypercube Sampling (LHS) [48] to generate multiple pairs of ϵ_{cc} and σ_{cc} in different regions of the parameter space, as detailed in the Results and Discussion Section.

For each row in the experimental design matrix obtained from LHS, we computed the CO_2 mass density (ρ_{CO_2}) and enthalpy of vaporization (ΔH_{vap}). We performed NPT simulations of 64,000 CO_2 molecules at 22.3 atm and 258 K to obtain these two quantities. The mass density was obtained from LAMMPS as the ratio of the mass of all the CO_2 atoms to the volume of the simulation domain. In contrast, the enthalpy of vaporization (ΔH_{vap}) was estimated as follows:

$$\Delta H_{vap} = H_g(GERG) - H_l(\epsilon_{cc}, \sigma_{cc}), \tag{4}$$

where the enthalpy of the CO_2 gas (H_g) was computed using the GERG (Group Europeén de Recherches Gazières) 2008 Equation of State (EOS) [49], whereas the enthalpy of the CO_2 liquid (H_l) was calculated from molecular simulations.

To find the optimum values of ϵ_{cc} and σ_{cc}, we computed the absolute relative error (ARE) as the absolute value of the difference between the model estimates of ρ_{CO_2} and ΔH_{vap}, and their corresponding experimental values. These experimental values were obtained from Harris and Yung [29] at 22.3 atm and 258 K. The experimental values of ρ_{CO_2} and ΔH_{vap} are 1.0061 gr/cc and 12.07 Kcal/mol, respectively. We defined a Weighted Objective Function (WOF) by combining the AREs of ρ_{CO_2} and ΔH_{vap} using the Lagrange multiplier $w_{\Delta H_{vap.}}$:

$$WOF = (w_{\Delta H_{vap.}})ARE_{\Delta H_{vap.}} + (1 - w_{\Delta H_{vap.}})ARE_{\rho_{CO_2}} \tag{5}$$

By setting $w_{\Delta H_{vap.}} = 0.8$ in Eq. (5), we assigned more weight to the enthalpy of vaporization because of its importance in accurately predicting phase change energies. To ensure accurate generation of CO_2's structural properties, we compared the CO_2–CO_2 Radial Distribution Function (RDF) obtained using the optimal SW potential parameters with the RDF generated using the all-atom EPM2-flex model Chen et al. [46]. The calculation of the RDF and its resulting plots are provided in Section S1 of the supplementary material provided. The results show a close match between the RDF of the coarse-grained SW and the all-atom EPM2 flex models.

2.3.2. Approach to calibrate the SW model for water–CO_2 interactions

Finding the optimum values of ϵ_{oc} and σ_{oc} involves computing the free energy (F), enthalpy of dissociation (ΔH_{diss}), CO_2 solubility in water (x_{CO_2}), and dissociation temperature (T_{diss}). These properties were calculated for each pair of (ϵ_{oc}, σ_{oc}) and compared to their experimental counterparts. The experimental conditions used to optimize the intermolecular potential parameters are overlaid as yellow and green dots on the CO_2 hydrate phase plot in Fig. 1. These two experimental conditions lie along the Water-Hydrate-Gas (WHG) curve. We obtained the experimental values for the enthalpy of dissociation and CO_2 solubility from Sabil et al. [50] and Chapoy et al. [51], respectively. The methods to compute these physicochemical properties from the coarse-grained MD simulations are explained as follows:

- **Free Energy (F)**: For computational efficiency, we employed a non-equilibrium approach to compute the free energy of solid hydrates.Jarzynski [53] related the equilibrium free energy difference and the irreversible work along a non-equilibrium path connecting the two equilibrium states, as follows:

  $$\Delta F = -\beta^{-1} \ln \overline{exp(-\beta W^{irr})}, \tag{6}$$

  where ΔF is the equilibrium free energy difference, $\beta = 1/(k_B T)$, k_B is the Boltzmann constant, T is temperature, and W^{irr} is the

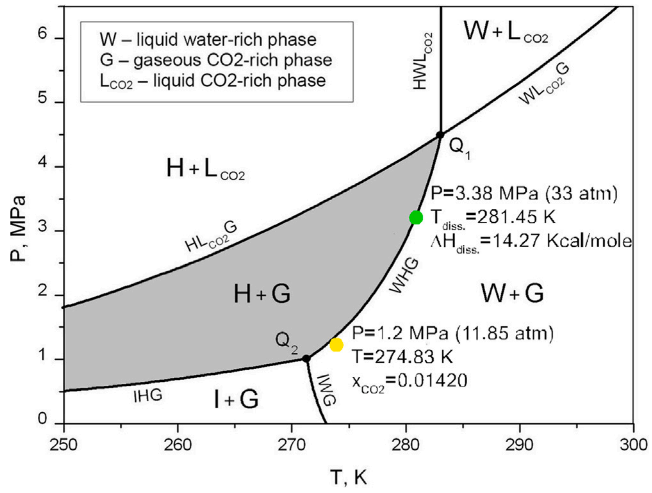

Fig. 1. Image shows an overlay of the experimental conditions used in calibrating the H_2O-CO_2 intermolecular potentials on the CO_2 phase plot from Voronov et al. [52]. The green dot represents the experimental conditions for ΔH_{diss} and T_{diss}, whereas the yellow dot represents the experimental conditions for CO_2 solubility.

irreversible work. The overline denotes the ensemble average of $exp(-\beta W^{irr})$. The free energy difference and the reversible work can be obtained from the ensemble average of the forward and backward irreversible works, as follows [54]:

$$\Delta F = F_2 - F_1 \equiv W_{rev} = \frac{1}{2}[\overline{W^{irr}}_{1\to2} - \overline{W^{irr}}_{2\to1}], \tag{7}$$

where $\overline{W^{irr}}_{1\to2}$ and $\overline{W^{irr}}_{2\to1}$ are irreversible works calculated in forward and backward non-equilibrium transitions, respectively. We employed the Frenkel–Ladd path described in Khanna et al. [55] to calculate the free energy of CO_2 hydrates, starting from the constrained Einstein crystals, as follows:

$$\beta F = \sum_i^N \ln\left(\frac{\beta k_i \Lambda_i^2}{2\pi}\right)^{3/2} + \beta\int_{\lambda=0}^{\lambda=1}\left\langle\frac{dU}{d\lambda}\right\rangle_\lambda^{CM} d\lambda - \ln\left[\left(\frac{\beta}{2\pi\sum_i^N \frac{\mu_i^2}{k_i}}\right)^{3/2}\left(\frac{V}{N_{mol}}\right)\right], \tag{8}$$

where F is the normalized free energy of hydrate, N_{mol} is the number of molecules, N is the number of atoms, h is the Planck's constant, m_i is mass of the ith atom, k_i is the spring constant for the ith atom, V is volume, U = potential energy, and λ is a coupling parameter between 0 and 1. Superscript CM indicates that the computation is center-of-mass constrained, and symbol Λ_i is defined as: $\Lambda_i = \left(\frac{\beta h^2}{2\pi m_i}\right)^{1/2}$. The integral $\int_{\lambda=0}^{\lambda=1}\left\langle\frac{dU}{d\lambda}\right\rangle_\lambda^{CM} d\lambda$ denotes the free energy difference between the CM Einstein crystal and the CM hydrate crystal. It is essentially the reversible work between the two states and is calculated from Eq. (7) through non-equilibrium integration. The forward and backward $\overline{W^{irr}}$ in Eq. (7) are calculated by perturbing the potential energy of the system along the path parameterized by λ [56]:

$$\overline{W^{irr}}_{1\to2} = \int_0^{t_s} dt\frac{d\lambda}{dt}\frac{\partial H}{\partial \lambda}. \tag{9}$$

To determine hydrate's free energy for each pair of (ϵ_{oc}, σ_{oc}), we simulated a supercell with $5 \times 5 \times 5$ s_I unit cells in the x, y, and z directions, respectively. We performed NPH simulations for 0.5 ns, using a Langevin thermostat to equilibrate the system to 250 K at a pressure of 33 atm. At this condition, we expect a CO_2–water mixture to exist in the solid hydrate state based on Fig. 1 [52]. From the NPH simulations, we determined the spring constants (k_i in Eq. (8)) for CO_2 and H_2O molecules. Next, we performed NVE simulations to transition the system between the current state and the Einstein crystal in both forward and backward directions. The spring constants calculated in the NPH simulations were used to improve the accuracy and speed of the perturbation simulations. The energy differences were determined along the non-equilibrium paths and used to calculate the forward and backward irreversible works. The irreversible works were then used in Eq. (7) to determine the center-of-mass constrained free energy difference, which is essentially the $\int_{\lambda=0}^{\lambda=1}\left\langle\frac{dU}{d\lambda}\right\rangle_\lambda^{CM} d\lambda$ term in Eq. (8). Freitas et al. [56] provides further details on its implementation in LAMMPS.

- **Enthalpy of Dissociation** (ΔH_{diss}): The enthalpy of dissociation of CO_2 hydrates is essentially the difference between the enthalpy of a solid CO_2 hydrate and that of its constituent liquid water and gaseous CO_2 molecules. Mathematically, it is computed as follows:

$$\Delta H_{diss} = 5.75H_{H_2O(l)} + H_{CO_2(g)} - H_{CO_2\cdot 5.75H_2O(s)}, \tag{10}$$

where $H_{H_2O(l)}$ represents the enthalpy of liquid water, $H_{CO_2(g)}$ represents the enthalpy of gaseous CO_2, and $H_{CO_2\cdot 5.75H_2O(s)}$ corresponds to the enthalpy of solid CO_2 hydrate. To estimate $H_{H_2O(l)}$, we performed NVT equilibration for 2 ns, followed by a 10 ns NPT simulation of a system with 46,000 water molecules. For $H_{CO_2(g)}$, we performed NVT equilibration for 2 ns, followed by a 10 ns NPT simulation of a system with 2744 CO_2 molecules. Finally, to estimate the enthalpy of the CO_2 hydrate, we performed NVT equilibration for 2 ns, followed by a 10 ns NPT simulation of a supercell with $7 \times 7 \times 7$ s_I unit-cells.
In addition to the coarse-grained MD simulations discussed, we performed three different AA MD simulations to determine the ΔH_{diss} components at the atomistic level. For $H_{H_2O(l)}$, we performed NVT equilibration for 2 ns, followed by a 10 ns NPT simulation of a system with 2944 water molecules. For $H_{CO_2(g)}$, we performed NVT equilibration for 2 ns, followed by a 10 ns NPT simulation of a system with 512 CO_2 molecules. For $H_{CO_2\cdot 5.75H_2O(s)}$, we performed NVT equilibration for 2 ns, followed by a 10 ns NPT simulation of a solid hydrate system with 2944 H_2O and 512 CO_2 molecules.
- **CO_2 solubility in water** (x_{CO_2}): To determine the CO_2 solubility in water, we first generated a system of CO_2 hydrates with $20 \times 4 \times 4$ s_I unit cells. We brought this system to equilibrium by running NVT and NPT simulations at 250 K and 33 atm. Next, we divided the simulation domain into four quarters (from left to right). We removed all the water molecules in the first and the last quarters and all the CO_2 molecules in the middle of the domain. We then melted the entire system by performing NVT simulations at 450 K for 5 ns and obtained a water–CO_2 two-phase mixture. Finally, we performed NPT simulations for 100 ns at the desired pressure and temperature conditions to obtain the CO_2 solubility. Using the plots of the phase densities of water and CO_2, the CO_2 solubility in water (x_{CO_2}) was calculated in the water-enriched phase as follows:

$$x_{CO_2} = \frac{n_{CO_2}}{n_{CO_2} + n_{H_2O}} = \frac{c_{CO_2}}{c_{CO_2} + c_{H_2O}}, \tag{11}$$

where the second form of the equation is used because the molar densities of CO_2 and water (c_{CO_2} and c_{H_2O}) are readily obtained by dividing ρ_{CO_2} and ρ_{H_2O} by the molecular weights of CO_2 and water, respectively. The symbol n represents the number of moles.
- **Dissociation Temperature** (T_{diss}): We used the direct-coexistence method [57] to determine the dissociation (melting or equilibrium) temperature (T_{diss}) of CO_2 hydrate. To this end, we first created a system with $12\times 6 \times 6$ s_I unit cells of CO_2 hydrates. We then melted only the first (left) and last (right) quarters of the simulation box by imposing a higher temperature of 450

K via a 100 ns NVT simulation that leaves the middle region intact. Finally, we performed several 0.6 μs NPT simulations at 33 atm but at different temperatures to determine the temperature at which the hydrate/liquid interface remains stationary. This temperature is the dissociation temperature (T_{diss}) of the CO_2 hydrate at the specified pressure.

In addition to estimating T_{diss} for CG systems, as described in the preceding paragraph, we estimated T_{diss} for the AA model in a similar manner. This involved creating an AA hydrate supercell with 8 × 4 × 4 s_I unit cells. Next, we melted the first and last quarter of the simulation box by performing an NVT simulation at 450 K over only this region for 5 ns, leaving the hydrates in the middle region intact. Finally, we performed several 100 ns NPT simulations at the specified equilibrium pressure but at different temperatures to determine T_{diss}.

The procedure to find the optimum values of ϵ_{oc} and σ_{oc} are summarized as follows:

1. Generate 2000 pairs of ϵ_{oc} (between 0.1 and 0.8) and σ_{oc} (between 3 and 5) using LHS.
2. For each pair of ϵ_{oc} and σ_{oc}, compute the free energy and plot all 2000 pairs as a map against the ϵ_{oc} and σ_{oc} on the x- and y-axes.
3. Select two regions of low free energy based on the map created in (2) above. Using LHS for each region, generate at least 250 new pairs of ϵ_{oc} and σ_{oc}.
4. Simulate all realizations in the LHS design matrix and generate a map of the enthalpy of dissociation (ΔH_{diss}) in these two regions.

2.4. Large-scale CO_2 hydrate simulation systems studied

After finding the optimal CG intermolecular potential parameters, we set up two large-scale simulations to study CO_2 hydrate growth. In the first setup, which serves as the basis of most of the rest of this paper, we created a simulation box with 80 × 10× 10 s_I unit cells of CO_2 hydrate in x, y, and z directions, respectively. This results in a system with 432,000 molecules and an initial dimension of 96 nm × 12 nm × 12 nm. The second setup consists of 160 × 20× 20 s_I unit cells with an initial dimension of 192 × 24× 24 nm. Volumetrically, the second system is eight times larger than the base case, consisting of 3.456 million molecules.

To generate the initial configuration for hydrate formation simulations, we first equilibrated the CO_2 hydrate crystals at 33 atm and 250 K via an NVT simulation for 500 ps, followed by an NPT simulation for 1 ns. Next, we divided the simulation domain into four quarters (from left to right). We melted the first and the last quarters of the domain by running NVT simulations for 5 ns at a melting temperature (T_m) higher than the dissociation temperature (T_{diss}) of CO_2 hydrate at 33 atm. This generated a multi-phase solid/liquid/gas system, which was the initial configuration for the subsequent large-scale NPT formation simulations. All NPT hydrate growth simulations were performed at the fixed pressure of 33 atm but variable formation temperatures (T_f).

2.5. Post-processing of simulation results

In addition to using Visual Molecular Dynamics (VMD) [58] to visualize the trajectories and Paraview [59] to map the simulation outputs over the intermolecular potential parameters, we developed in-house codes to post-process the simulation results. We developed a C++ code based on the GRADE algorithm [60] to detect and track the hydrate motifs in the simulation domain. We extended the GRADE algorithm to identify the $5^{12}6^3$ cages, which are essential in the growth of s_I hydrate structures, as explained in Walsh et al. [26]. The cage identification code is publicly accessible at https://github.com/UnconvRS/CageIdentification, whereas other codes developed as part of this work can be cloned at https://github.com/UnconvRS/CO2HydrateMD. To study the kinetics of CO_2 hydrate growth, we track the evolution of the hydrate mass during the simulations using our open-source implementation of an approach [44] based on the template-matching algorithm [61]. Finally, we developed a Python package to extract and map the simulation outputs over the intermolecular potential parameters (ϵ and σ) on the x and y axes, respectively.

3. Results and discussion

3.1. CG CO_2–CO_2 potential parameters

This section presents the results of our efforts to calibrate the SW intermolecular potential for CO_2–CO_2 interactions. We generated 500 different pairs of ϵ_{cc} and σ_{cc} using LHS as described in the previous section. These realizations covered a wide range of values (between 0.1 and 0.8 Kcal/mol) for ϵ_{cc} and (between 3 and 5 Å) for σ_{cc}. For each of these 500 realizations, we obtained ρ_{CO_2} directly from LAMMPS and computed ΔH_{vap} as explained in Eq. (4).

The maps in Fig. 2(a–c) show the plots of $ARE_{\rho_{CO_2}}$, $ARE_{\Delta H_{vap}}$, and WOF against these 500 ϵ_{cc} and σ_{cc} pairs at the vapor–liquid coexistence conditions of 22.3 atm and 258 K. The ARE map for ρ_{CO_2} indicates that the optimal σ_{cc} is between 4.0 and 4.5 Å, whereas the ARE map for ΔH_{vap} does not provide any constraint on the optimal range for σ_{cc}. $ARE_{\rho_{CO_2}}$ indicates that the optimal ϵ_{cc} value is greater than 0.5 Kcal/mol, whereas $ARE_{\Delta H_{vap}}$ indicates that the optimal ϵ_{cc} value is between 0.6 and 0.7 Kcal/mol. The WOF map mostly follows the trend for $ARE_{\Delta H_{vap}}$.

Learning from the ARE plots for the initial 500 LHS realizations of ϵ_{cc} and σ_{cc}, we narrowed down the sampling range for these parameters to lie between 0.5 and 0.8 Kcal/mol for ϵ_{cc} and between 3.9 and 4.4 Å for σ_{cc}. Using LHS, we generated 300 new pairs of ϵ_{cc} and σ_{cc} over this refined region, computed their corresponding $ARE_{\rho_{CO_2}}$, $ARE_{\Delta H_{vap}}$, and WOF, and plotted them in Fig. 2-(d–f). Using the WOF map, we identified the optimal CG-SW potential parameters as ϵ_{cc}^{opt} = 0.64 Kcal/mol and σ_{cc}^{opt} = 4.25 Å for the CO_2–CO_2 interactions. The AREs for the optimal potential parameters are summarized in Table 1.

3.2. CG Water-CO_2 potential parameters

This section presents the results of our efforts to calibrate the SW intermolecular potential for water–CO_2 interactions. We used the optimized CO_2–CO_2 interaction parameters obtained from the previous subsection in all the simulations performed to find the optimal water–CO_2 interaction terms. First, we generated the stability map of CO_2 hydrates by mapping the free energy of hydrate crystals over 2000 pairs of ϵ_{oc} (between 0.1 and 0.8 Kcal/mol) and σ_{oc} (between 3 and 5 Å). This stability map serves as a reference for refining the intermolecular potentials to match the experimental data available on the physicochemical properties discussed in the Materials and Methods Section.

The normalized free energy of the CO_2 hydrate calculated from Eq. (8) at 33 atm and 250 K is plotted against ϵ_{oc} and σ_{oc} in Fig. 3. It indicates that the most stable hydrate structures lie within the wedge-like region with the lowest free energy values. This region (referred to as Region I in Fig. 3) is bounded by ϵ_{oc} values between 0.2 and 0.3 Kcal/mol and by σ_{oc} values between 3.0 to 4.5 Å. In addition to the minimization of the free energy, calibrating ϵ_{oc} and σ_{oc} involves matching other physicochemical properties (ΔH_{diss}, x_{CO_2}, and T_{diss}). So, instead of simply focusing on Region I, we also selected a second region (Region II), which is bounded by ϵ_{oc} values between 0.3 and 0.8 Kcal/mol and by σ_{oc} values between 3.0 to 4.5 Å. Using LHS, we generated 250 pairs of ϵ_{oc} and σ_{oc} in Region I and 1000 pairs in Region II.

The enthalpy of dissociation was calculated for all the ϵ_{oc} and σ_{oc} pairs in both regions and the $ARE_{\Delta H_{diss}}$ was calculated relative to the

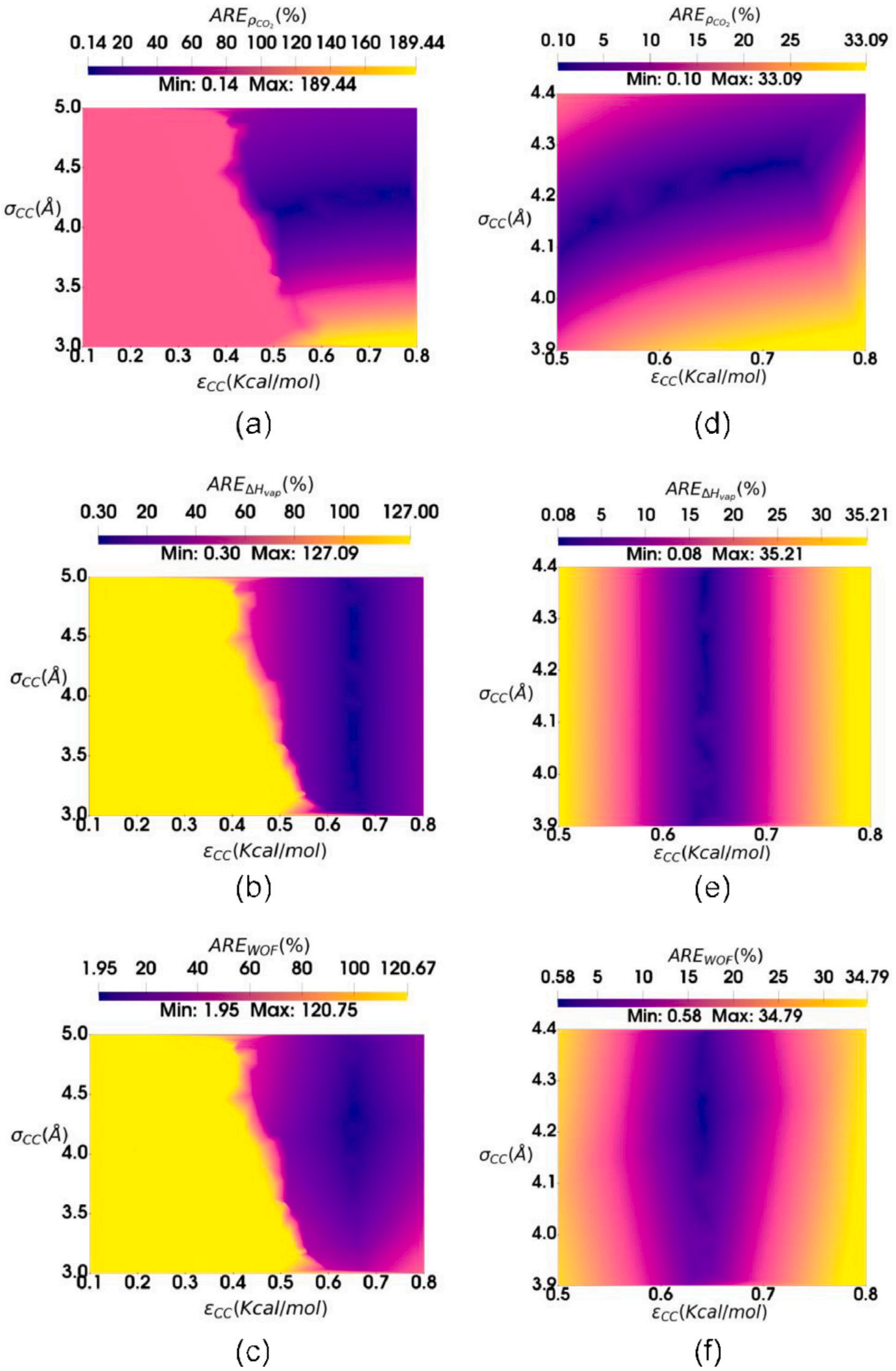

Fig. 2. The profiles in (a–c) present the (a) ARE of ρ_{CO_2}, (b) ARE of ΔH_{vap}, and (c) ARE of the WOF over the preliminary force field region; whereas the profiles in (d–f) present the (d) ARE of ρ_{CO_2}, (e) ARE of ΔH_{vap}, and (f) ARE of the WOF over the refined region.

Table 1
Summary of the $ARE_{\rho_{CO_2}}$, $ARE_{\Delta H_{vap}}$, and WOF of the optimal CO_2–CO_2 potential.

$\epsilon_{cc}^{opt.}$ (Kcal/mol)	$\sigma_{cc}^{opt.}$ (Å)	ρ_{CO_2} (gr/cc)	$ARE_{\rho_{CO_2}}$ (%)	$\Delta H_{vap.}$ (Kcal/mol)	$ARE_{\Delta H_{vap.}}$ (%)	WOF (%)
0.64	4.25	0.9880	1.80	2.87	0.28	0.58

experimental values from Sabil et al. [50]. The $ARE_{\Delta H_{diss}}$ is plotted against ϵ_{oc} and σ_{oc} in Fig. 4 for both regions. In general, Region II has a smaller minimum ARE of only 0.05% compared to the minimum $ARE_{\Delta H_{diss}}$ of 39.13% in Region I. The minimal ARE appears in a wedge-like area for both regions, like in the free energy map presented in Fig. 3.

Table 2

Estimated ΔH_{diss}, x_{CO_2}, T_{diss} values and corresponding ARE values for the optimum potential from Region I.

ϵ_{oc} (Kcal/mol)	σ_{oc} (Å)	ΔH_{diss} (Kcal/mol)	$ARE_{\Delta H_{diss}}$ (%)	x_{CO_2} (mole fraction)	$ARE_{x_{CO_2}}$	T_{diss} (K)	$ARE_{T_{diss}}$ (%)	ΔS_{diss} (cal/mole/K)	$ARE_{\Delta S_{diss}}$ (%)
0.20	3.21	5.89	58.79	0.01473	3.76	289.0	2.68	20.35	59.86

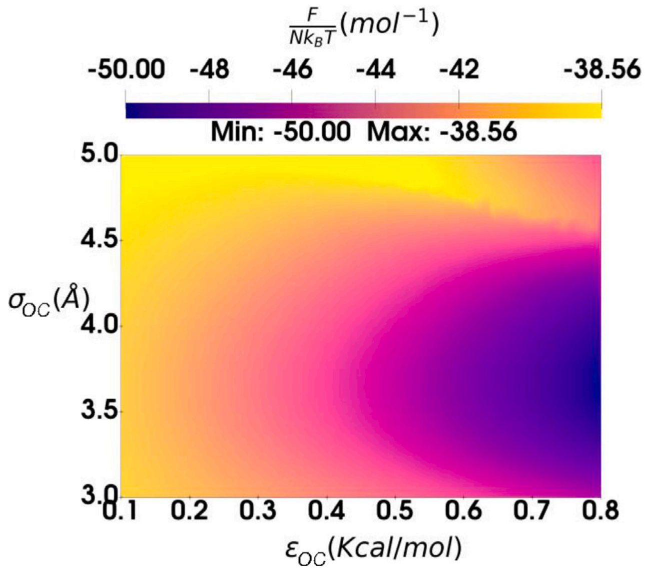

Fig. 3. This map shows the normalized free energy ($\frac{F}{Nk_BT}$) of CO_2 hydrate crystals relative to the Einstein crystal (at 33 atm and 250 K) plotted against ϵ_{OC} and σ_{OC}.

Next, we selected multiple points from Regions I and II to determine the CO_2 solubility (x_{CO_2}) atp = 11.85 atm and T = 274.83 K, as shown in Fig. 1. The calculated x_{CO_2} values were then compared to the experimental x_{CO_2} values from Chapoy et al. [51]. Although the areas with low $ARE_{\Delta H_{diss}}$ values in Region II have lower values than in Region I, the x_{CO_2} values estimated for the points in Region I were generally more accurate than those from Region II. This is consistent with the results presented by Jacobson and Molinero [43] on calibrating the SW potential for coarse-grained methane hydrate simulation studies. Like Jacobson and Molinero [43], we prioritized accurate estimations of CO_2 solubility over the free energy and $ARE_{\Delta H_{diss}}$ values because hydrate formation depends on the number of available gas molecules in water. So, the subsequent calculations of the dissociation temperature were limited to the promising points in Region I.

To estimate the dissociation temperature, we chose the intermolecular potential with the lowest $ARE_{x_{CO_2}}$ in Region I. We estimated the CO_2 solubility using the density profile presented in Figure S2 of the supplementary material. The results obtained using the selected potential are summarized in Table 2. In general, the ϵ_{oc} and σ_{oc} values are much less than the ϵ_{cc} and σ_{cc} values. This lower value of σ_{oc} can be attributed to the smaller effective radius of water molecules compared to CO_2 molecules.

From Table 2, we observe that this intermolecular potential has a low ARE in the CO_2 solubility and dissociation temperature, but the ARE of the dissociation enthalpy is high. As explained in Jacobson and Molinero [43], it is impossible to accurately estimate both ΔH_{diss} and T_{diss} using a CG model because of the omission of the rotational term in the entropy of dissociation (ΔS_{diss}). The entropy of dissociation is related to ΔH_{diss} and T_{diss} as follows:

$$\Delta S_{diss} = \frac{\Delta H_{diss}}{T_{diss}}. \tag{12}$$

Table 3

A comparison of AREs from CG and AA models.

	CG-SW	AA-EPM2-flex/TIP4P-ice
ϵ_{oo} (Kcal/mol)	6.189	–
σ_{oo} (Å)	2.3925	–
λ_w	23.15	–
ϵ_{cc} (Kcal/mol)	0.64	–
σ_{cc} (Å)	4.25	–
ϵ_{oc} (Kcal/mol)	0.20	–
σ_{oc} (Å)	3.21	–
$ARE_{\Delta H_{diss}}$	58.79%	57%
$ARE_{T_{diss}}$	2.68%	0.7%
$ARE_{\Delta S_{diss}}$	59.86%	57%

For completeness, we also reported the ARE in the enthalpy of dissociation ($ARE_{\Delta S_{diss}}$) in Table 2. Finally, we compared the performance of our optimal CG-SW intermolecular potential with the AA model discussed in the Materials and Methods Section. We used the same methods and techniques for calibrating the CG potential to determine the enthalpy of dissociation, dissociation temperature, and the entropy of dissociation in the AA system. The estimated values from the CG and AA systems are compared in Table 3. Although the AA model outperforms the CG model in T_{diss} estimation, it yields almost the same accuracy in estimating ΔH_{diss}. The AA model is only 2% more accurate than the CG model in estimating ΔS_{diss}. This indicates that our calibrated CG model is roughly as accurate as the AA model in capturing the changes in the molecular randomness due to hydrate dissociation.

3.3. Large-scale CO_2 hydrate growth studies

Using the optimized CG model parameters summarized in Table 3, we performed several large-scale simulations to study CO_2 hydrate growth. Table 4 summarizes our ten simulations and their corresponding conditions and domain sizes. For the main (96 nm × 12 nm × 12 nm) simulation box, we repeated these CG hydrate simulations starting from four different initial (velocity distribution) conditions. We refer to these repeated cases as simulation replicates for brevity. We simulated the first replicate at 250, 260, and 270 K, whereas the other three replicates were simulated at 250 and 260 K. This table shows that the pressure was maintained at 33 atm in all 10 cases.

3.3.1. Analysis of CO_2 hydrate growth at 250 K

Fig. 5 shows how the CO_2 hydrate grows over time as the temperature drops from the equilibrium temperature of 289 K (for the optimized SW potential) to 250 K. The first snapshot at 0 μs (in Fig. 5a) shows the initial system configuration, whereas the last snapshot at 0.13 μs (in Fig. 5e) shows when the hydrate was fully formed and the interface was no longer moving. The other snapshots shown in Fig. 5(b,c,d) correspond to the times when 25%, 50%, and 75% of the hydrates in Fig. 5(e) were formed. A movie showing the growth of the hydrate over time at 250 K is provided at https://youtu.be/11s3bdxaE7Q as Movie S1 in the supplementary materials. As expected, the solid hydrate grows outward from the solid region bounded by the dotted yellow lines towards the fluid region. The results indicate that the CO_2 nanobubbles on either side of the solid hydrate get trapped within the hydrate as the hydrates grow to engulf it.

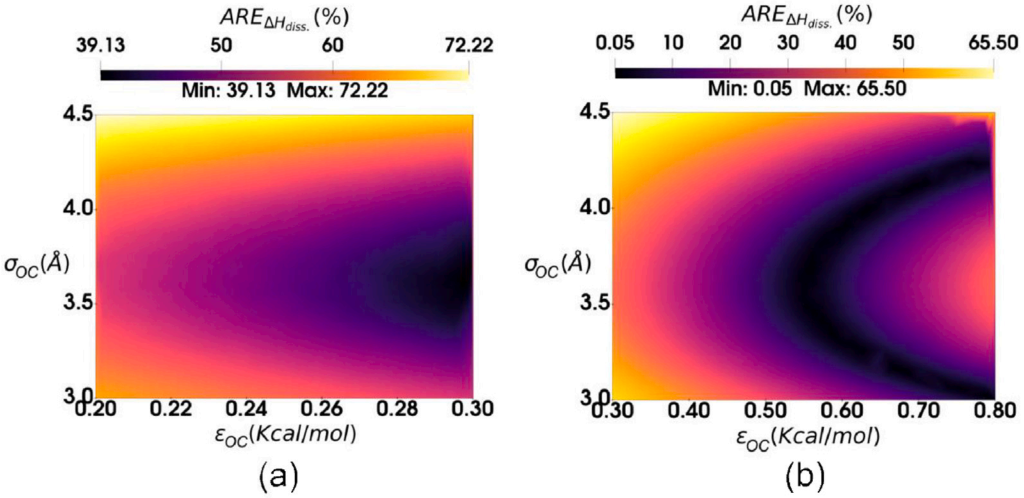

Fig. 4. This figure shows the map of the $ARE_{\Delta H_{diss}}$ in (a) Region I and (b) Region II at 33 atm and 250 K.

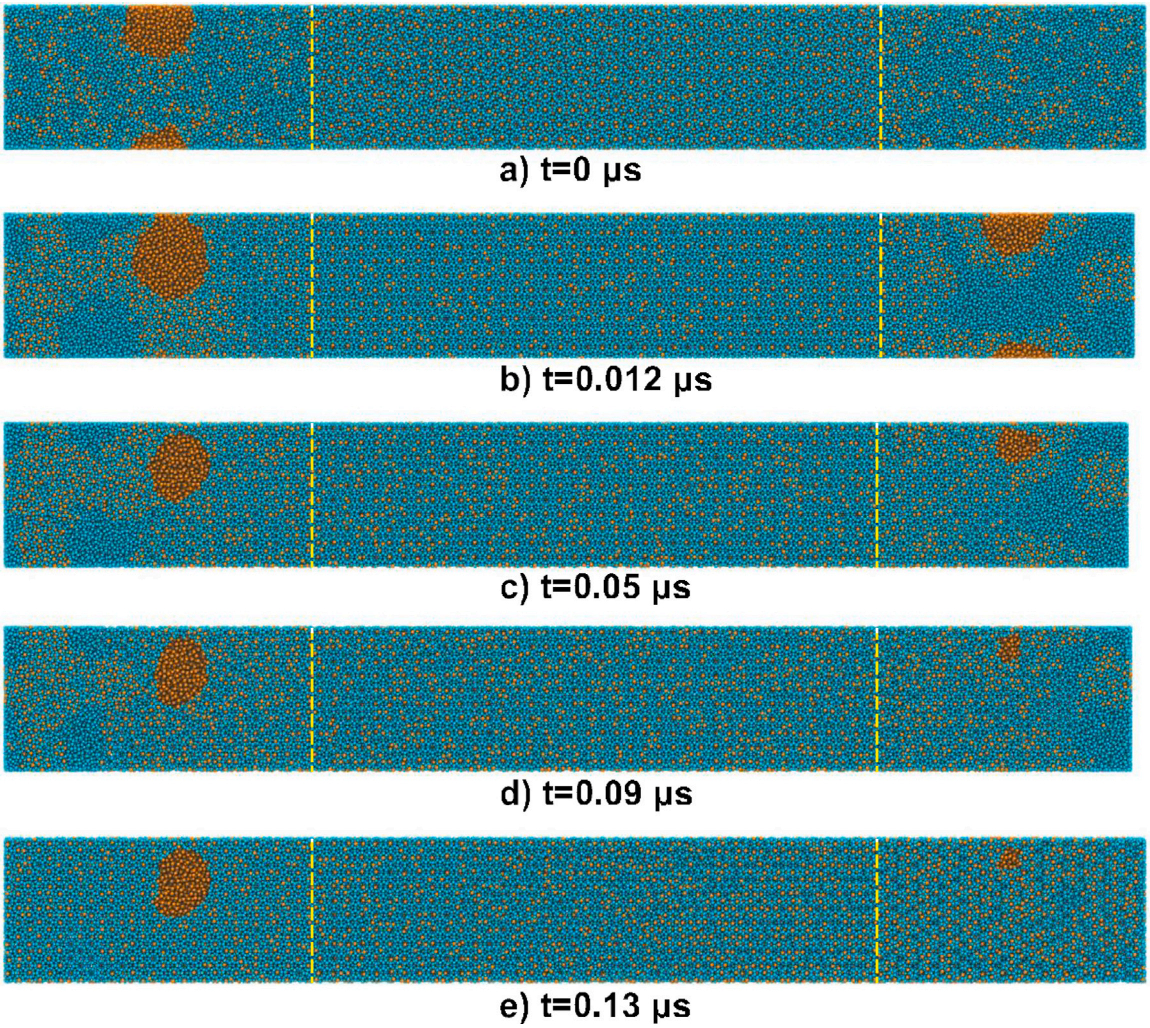

Fig. 5. These results show the snapshots of the molecular trajectories for case 1 when (a) 0%, (b) 25%, (c) 50%, (d) 75%, and (e) 100% of the hydrates are formed. Cyan spheres represent water molecules, orange spheres represent CO_2 molecules, and the dotted yellow lines indicate the location of the initial solid/liquid interface.

Table 4
Summary of the CG MD simulations performed to study CO_2 hydrate growth.

p (atm)	Box dimensions (nm x nm x nm)	Replicate	T_m(K)	T_f (K)	Case
33	96 × 12 × 12	1	450	250	1
				260	2
				270	3
		2	465	250	4
				260	5
		3	480	250	6
				260	7
		4	495	250	8
				260	9
	192 × 24 × 24	1	450	250	10

To the best of the authors' knowledge, the observation of the trapping of CO_2 nanobubbles within a solid hydrate during hydrate formation has never been reported in the literature. This could be attributed to the fact that the nanobubble is bigger than the simulation domain used in most of the previous all-atom MD simulations of gas hydrates. To understand the mechanism by which the nanobubble gets trapped, Fig. 6 provides a closer look at the results from the case presented in Fig. 5. At t=0, the CO_2 nanobubble is surrounded by water with dissolved CO_2 molecules, and the initial solid/liquid interface is at the position of the dotted yellow line in Fig. 6(a). As time evolves and the temperature drops from the equilibrium temperature of 289 K to 250 K, hydrates begin to form, and the solid/liquid interface advances to the right side of the nanobubble. The dissolved CO_2 molecules also reorient themselves around the CO_2 nanobubble as in Fig. 6(b). Looking to the right side of the nanobubble, we notice the formation of both fully occupied and partially filled gas hydrate structures. This indicates that the rate of hydrate growth is faster than the mass rate at which the CO_2 is transferred to the growing hydrate interface. A movie showing the close-up view of the CO_2 hydrate growth over time is provided at https://youtu.be/bys1YtrAfuY as Movie S2 in the supplementary materials.

As detailed in Section S-4 of the supplementary file, we computed the mass density of the CO_2 in the trapped nanobubble and that in the s_I hydrate structure at t = 0 ns, and obtained 0.95 gcc and 0.38 gcc, respectively. So, the amount of CO_2 (per unit volume) trapped as a nanobubble within the solid hydrate is 2.5 times its standard amount in a s_I hydrate. This implies that the storage potential of CO_2 in hydrates could be significantly enhanced by forming and trapping CO_2 nanobubbles within the solid hydrate cages.

In addition to the results presented for case 1, Figures S4 and S5 and their corresponding movies (Movies S3 and S4) in the supplementary material present the corresponding snapshots of the hydrate growth for cases 2 and 3. By comparing the results for cases 1 through 3, we obtained insights into the effect of temperature on CO_2 hydrate growth. Although these three cases had the same initial configuration, they were subjected to different temperatures (250, 260, and 270 K). As expected, the rate of hydrate growth was faster at 250 K than at 260 K, which was faster than at 270 K.

3.3.2. *Verification of nanobbuble trapping in solid hydrates*

Considering the significance of our observation of the trapping of CO_2 nanobubbles within the solid hydrate, this section focuses on verifying that the observation is reproducible at different initial conditions and in larger simulation domains. To this end, we repeated the coarse-grained simulations using different initial conditions by melting the left and right quarters at various temperatures (T_m), as shown in Table 4. Hydrate growth at 270 K was very slow (as shown in Figure S5), so the replicates were set up only at 250 and 260 K. The seed used to initialize the velocity was also changed in each replica to ensure randomness. Cases 4, 6, and 8 are the replicas of case 1 at 250 K, whereas cases 5, 7, and 9 are the replicas of case 2 (presented in Figure S4) at 260 K. Visualizing these cases shows that CO_2 nanobubbles were trapped within the solid hydrate in all replicates with CO_2 nanobubbles after melting the left and right regions of the domain.

In addition to verifying nanobubble trapping in the solid hydrate by analyzing the effect of different initial conditions, we simulated a system eight times larger than the domain used in cases 1 to 9. The number of s_I unit cells in the supercell of case 10 is 160 × 20 × 20 in the x, y, and z dimensions, respectively, resulting in a system with initial dimensions of 192 × 24 × 24 nm. To our knowledge, this is by far the largest MD simulation performed for gas hydrate studies. The molecular trajectories presented in Fig. 7 justify the trapping of CO_2 nanobubbles within the newly formed hydrate also in this large-scale simulation. Therefore, the verification studies indicate that the trapping of CO_2 nanobubbles within solid hydrates is not limited to a few initial configurations or small domains.

4. Conclusions

We calibrated the Stillinger–Weber potential using experimental and all-atom MD simulation results to accurately and efficiently model CO_2–CO_2 and Water–CO_2 interactions. The calibrated coarse-grained model was used to perform several large-scale MD studies of CO_2 hydrate growth. A rigorous analysis of the simulation results indicates that:

1. CO_2 can be trapped as nanobubbles within the growing solid hydrate.
2. the CO_2 density in the nanobubble was 2.5 times that in the solid hydrate, which indicates the game-changing potential of increasing hydrate-based CO_2 storage via nanobubbles.
3. At temperatures of 260 K or lower, we observed that the CO_2 hydrate growth rate was faster than the rate at which the CO_2 molecules diffused into the water.
4. the size of the CO_2 nanobubble was larger than the simulation domain used in most of the previous CO_2 hydrate studies. So, it is important to simulate large-scale systems to observe physical mechanisms occurring at scales larger than the typical all-atom MD simulation domains.

CRediT authorship contribution statement

Meisam Adibifard: Writing – original draft, Visualization, Validation, Software, Methodology, Investigation, Formal analysis, Data curation, Conceptualization. **Olufemi Olorode:** Writing – review & editing, Writing – original draft, Supervision, Software, Resources, Project administration, Methodology, Funding acquisition, Conceptualization.

Declaration of competing interest

The authors declare that they have no known competing financial interests or personal relationships that could have appeared to influence the work reported in this paper.

Acknowledgments

This material is based upon work supported by the U.S. Department of Energy, Office of Science, Office of Basic Energy Sciences, Geosciences program under Award Number DE-SC0024382. The authors acknowledge using the computational resources at the LSU Center for Computation and Technology (CCT). We also appreciate helpful discussions with Dr. Revati Kumar.

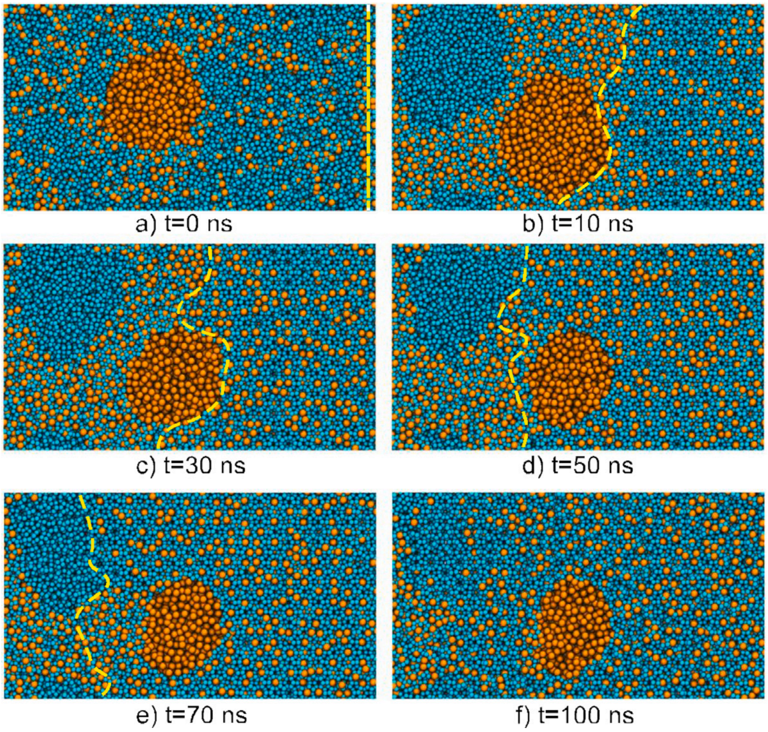

Fig. 6. These images show a closer look into how the nanobubble on the left side of the left solid/liquid interface is trapped in case 1. Cyan represents water molecules, while orange represents CO_2 molecules. The dotted yellow lines indicate the position of the solid/liquid interface at the specified time steps.

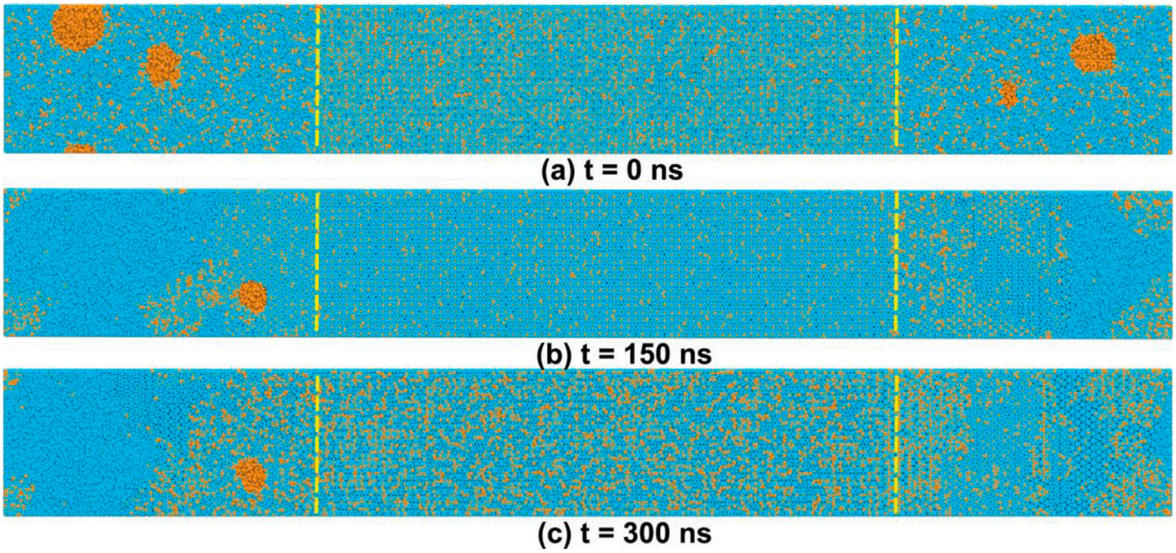

Fig. 7. Snapshots of the molecular trajectories for the first replicate of the larger simulation box (192 nm × 24 nm × 24 nm) atp = 33 atm and the sub-cooling temperature of$T$ = 250 K at the beginning (a), middle (b), and the end of the simulation (c). Cyan spheres represent water molecules, orange spheres represent CO_2 molecules, and the dotted yellow line locates the initial crystal/liquid interface.

Appendix A. Supplementary data

Supplementary material related to this article can be found online at https://doi.org/10.1016/j.mtsust.2025.101106.

Data availability

The codes developed as part of this study are openly available in the "CO_2 Hydrate" GitHub repository at https://github.com/UnconvRS/CO2HydrateMD. Other related data are available on request.

References

[1] E.D. Sloan Jr., C.A. Koh, Clathrate Hydrates of Natural Gases, CRC Press, 2007.

[2] J. Kondori, L. James, S. Zendehboudi, Molecular scale modeling approach to evaluate stability and dissociation of methane and carbon dioxide hydrates, J. Mol. Liq. 297 (2020) 111503.

[3] A. Graue, B. Kvamme, B. Baldwin, J. Stevens, J. Howard, E. Aspenes, G. Ersland, J. Husebø, D. Zornes, MRI visualization of spontaneous methane production from hydrates in sandstone core plugs when exposed to CO2, Spe J. 13 (02) (2008) 146–152.

[4] O.Y. Zatsepina, M. Pooladi-Darvish, CO2-hydrate formation in depleted gas reservoirs–a methodology for CO2 storage, Energy Procedia 4 (2011) 3949–3956.

[5] P.Y. Park YoungJune, K.D. Kim DoYoun, L.J. Lee JongWon, H.D. Huh DaeGee, P.K. Park KeunPil, L.J. Lee JaehYoung, L.H. Lee Huen, Sequestering carbon dioxide into complex structures of naturally occurring gas hydrates, 2006.
[6] J. Yang, P. Gong, R. Fu, M. Zhang, J. Chen, S. Liang, B. Xu, J. Shi, R. Dickinson, The role of satellite remote sensing in climate change studies, Nat. Clim. Chang. 3 (10) (2013) 875–883.
[7] D. Wuebbles, D. Fahey, E. Takle, K. Hibbard, J. Arnold, B. DeAngelo, S. Doherty, D. Easterling, J. Edmonds, T. Edmonds, et al., Climate science special report: Fourth national climate assessment (NCA4), volume I, 2017.
[8] B. Dziejarski, R. Krzyżyńska, K. Andersson, Current status of carbon capture, utilization, and storage technologies in the global economy: A survey of technical assessment, Fuel 342 (2023) 127776.
[9] P.K. Naraharisetti, T.Y. Yeo, J. Bu, New classification of CO2 mineralization processes and economic evaluation, Renew. Sustain. Energy Rev. 99 (2019) 220–233.
[10] A.J. Cavanagh, R.S. Haszeldine, The sleipner storage site: Capillary flow modeling of a layered CO2 plume requires fractured shale barriers within the utsira formation, Int. J. Greenh. Gas Control. 21 (2014) 101–112.
[11] P. Ringrose, M. Atbi, D. Mason, M. Espinassous, Ø. Myhrer, M. Iding, A. Mathieson, I. Wright, Plume development around well KB-502 at the in Salah CO2 storage site, First Break 27 (1) (2009).
[12] B. Kvamme, A. Graue, T. Buanes, T. Kuznetsova, G. Ersland, Storage of CO2 in natural gas hydrate reservoirs and the effect of hydrate as an extra sealing in cold aquifers, Int. J. Greenh. Gas Control. 1 (2) (2007) 236–246.
[13] J. Gauteplass, S. Almenningen, G. Ersland, T. Barth, J. Yang, A. Chapoy, Multiscale investigation of CO2 hydrate self-sealing potential for carbon geo-sequestration, Chem. Eng. J. 381 (2020) 122646.
[14] C. Le Quéré, R.M. Andrew, P. Friedlingstein, S. Sitch, J. Pongratz, A.C. Manning, J.I. Korsbakken, G.P. Peters, J.G. Canadell, R.B. Jackson, et al., Global carbon budget 2017, Earth Syst. Sci. Data 10 (1) (2018) 405–448.
[15] K.Z. House, D.P. Schrag, C.F. Harvey, K.S. Lackner, Permanent carbon dioxide storage in deep-sea sediments, Proc. Natl. Acad. Sci. 103 (33) (2006) 12291–12295.
[16] I. Fer, P.M. Haugan, Dissolution from a liquid CO2 lake disposed in the deep ocean, Limnol. Oceanogr. 48 (2) (2003) 872–883.
[17] H.J. Herzog, E.E. Adams, D. Auerbach, J. Caulfield, Environmental impacts of ocean disposal of CO2, Energy Convers. Manage. 37 (6–8) (1996) 999–1005.
[18] B. Metz, O. Davidson, H. De Coninck, M. Loos, L. Meyer, IPCC Special Report on Carbon Dioxide Capture and Storage, Cambridge University Press, Cambridge, 2005.
[19] A. Carroll, R. Przeslawski, L. Radke, J. Black, K. Picard, J. Moreau, R. Haese, S. Nichol, Environmental considerations for subseabed geological storage of CO2: A review, Cont. Shelf Res. 83 (2014) 116–128.
[20] Z.R. Chong, S.H.B. Yang, P. Babu, P. Linga, X.-S. Li, Review of natural gas hydrates as an energy resource: Prospects and challenges, Appl. Energy 162 (2016) 1633–1652.
[21] P. Englezos, Extraction of methane hydrate energy by carbon dioxide injection-key challenges and a paradigm shift, Chin. J. Chem. Eng. 27 (9) (2019) 2044–2048.
[22] P.G. Brewer, G. Friederich, E.T. Peltzer, F.M. Orr Jr., Direct experiments on the ocean disposal of fossil fuel CO2, Science 284 (5416) (1999) 943–945.
[23] J. Gabitto, D. Riestenberg, S. Lee, L. Liang, C. Tsouris, Ocean disposal of CO2: Conditions for producing sinking CO2 hydrate, J. Dispers. Sci. Technol. 25 (5) (2005) 703–712.
[24] C. Rochelle, A. Camps, D. Long, A. Milodowski, K. Bateman, D. Gunn, P. Jackson, M. Lovell, J. Rees, Can CO2 hydrate assist in the underground storage of carbon dioxide? Geol. Soc. Lond. Spec. Publ. 319 (1) (2009) 171–183.
[25] J. Zheng, Z.R. Chong, M.F. Qureshi, P. Linga, Carbon dioxide sequestration via gas hydrates: a potential pathway toward decarbonization, Energy & Fuels 34 (9) (2020) 10529–10546.
[26] M.R. Walsh, C.A. Koh, E.D. Sloan, A.K. Sum, D.T. Wu, Microsecond simulations of spontaneous methane hydrate nucleation and growth, Science 326 (5956) (2009) 1095–1098.
[27] B. Fang, F. Ning, W. Ou, D. Wang, Z. Zhang, Y. Yu, H. Lu, J. Wu, T.J. Vlugt, The dynamic behavior of gas hydrate dissociation by heating in tight sandy reservoirs: A molecular dynamics simulation study, Fuel 258 (2019) 116106.
[28] J. Abascal, E. Sanz, R. García Fernández, C. Vega, A potential model for the study of ices and amorphous water: TIP4P/Ice, J. Chem. Phys. 122 (23) (2005).
[29] J.G. Harris, K.H. Yung, Carbon dioxide's liquid-vapor coexistence curve and critical properties as predicted by a simple molecular model, J. Phys. Chem. 99 (31) (1995) 12021–12024.
[30] J.J. Potoff, J.I. Siepmann, Vapor–liquid equilibria of mixtures containing alkanes, carbon dioxide, and nitrogen, AIChE J. 47 (7) (2001) 1676–1682.
[31] H.A. Lorentz, Ueber die anwendung des satzes vom virial in der kinetischen theorie der gase, Ann. Phys., Lpz. 248 (1) (1881) 127–136.
[32] D. Berthelot, Sur le mélange des gaz, Compt. Rendus 126 (3) (1898) 15.
[33] Y.-T. Tung, L.-J. Chen, Y.-P. Chen, S.-T. Lin, Growth of structure I carbon dioxide hydrate from molecular dynamics simulations, J. Phys. Chem. C 115 (15) (2011) 7504–7515.
[34] Z. He, P. Linga, J. Jiang, What are the key factors governing the nucleation of CO 2 hydrate? Phys. Chem. Chem. Phys. 19 (24) (2017) 15657–15661.
[35] Y.-T. Tung, L.-J. Chen, Y.-P. Chen, S.-T. Lin, In situ methane recovery and carbon dioxide sequestration in methane hydrates: A molecular dynamics simulation study, J. Phys. Chem. B 115 (51) (2011) 15295–15302.
[36] Z. He, K.M. Gupta, P. Linga, J. Jiang, Molecular insights into the nucleation and growth of CH4 and CO2 mixed hydrates from microsecond simulations, J. Phys. Chem. C 120 (44) (2016) 25225–25236.
[37] Z. He, P. Linga, J. Jiang, CH4 hydrate formation between silica and graphite surfaces: insights from microsecond molecular dynamics simulations, Langmuir 33 (43) (2017) 11956–11967.
[38] Z. He, F. Mi, F. Ning, Molecular insights into CO2 hydrate formation in the presence of hydrophilic and hydrophobic solid surfaces, Energy 234 (2021) 121260.
[39] K.R. Hadley, C. McCabe, Coarse-grained molecular models of water: a review, Mol. Simul. 38 (8–9) (2012) 671–681.
[40] V. Molinero, E.B. Moore, Water modeled as an intermediate element between carbon and silicon, J. Phys. Chem. B 113 (13) (2009) 4008–4016.
[41] F.H. Stillinger, T.A. Weber, Computer simulation of local order in condensed phases of silicon, Phys. Rev. B 31 (8) (1985) 5262.
[42] E.B. Moore, V. Molinero, Structural transformation in supercooled water controls the crystallization rate of ice, Nature 479 (7374) (2011) 506–508.
[43] L.C. Jacobson, V. Molinero, A methane- water model for coarse-grained simulations of solutions and clathrate hydrates, J. Phys. Chem. B 114 (21) (2010) 7302–7311.
[44] M. Adibifard, O. Olorode, Large-scale nonequilibrium molecular studies of thermal hydrate dissociation, J. Phys. Chem. B 127 (29) (2023) 6543–6550.
[45] F. Takeuchi, M. Hiratsuka, R. Ohmura, S. Alavi, A.K. Sum, K. Yasuoka, Water proton configurations in structures I, II, and H clathrate hydrate unit cells, J. Chem. Phys. 138 (12) (2013).
[46] L. Chen, S. Wang, W. Tao, A study on thermodynamic and transport properties of carbon dioxide using molecular dynamics simulation, Energy 179 (2019) 1094–1102.
[47] A.P. Thompson, H.M. Aktulga, R. Berger, D.S. Bolintineanu, W.M. Brown, P.S. Crozier, P.J. in't Veld, A. Kohlmeyer, S.G. Moore, T.D. Nguyen, et al., LAMMPS-a flexible simulation tool for particle-based materials modeling at the atomic, meso, and continuum scales, Comput. Phys. Comm. 271 (2022) 108171.
[48] W.-L. Loh, On latin hypercube sampling, Ann. Statist. 24 (5) (1996) 2058–2080.
[49] O. Kunz, W. Wagner, The GERG-2008 wide-range equation of state for natural gases and other mixtures: an expansion of GERG-2004, J. Chem. Eng. Data 57 (11) (2012) 3032–3091.
[50] K.M. Sabil, Q. Nasir, B. Partoon, A.A. Seman, Measurement of H–LW–V and dissociation enthalpy of carbon dioxide rich synthetic natural gas mixtures, J. Chem. Eng. Data 59 (11) (2014) 3502–3509.
[51] A. Chapoy, A. Mohammadi, A. Chareton, B. Tohidi, D. Richon, Measurement and modeling of gas solubility and literature review of the properties for the carbon dioxide- water system, Ind. Eng. Chem. Res. 43 (7) (2004) 1794–1802.
[52] V. Voronov, E. Gorodetskii, V. Podnek, B. Grigoriev, Properties of equilibrium carbon dioxide hydrate in porous medium, Chem. Phys. 476 (2016) 61–68.
[53] C. Jarzynski, Nonequilibrium equality for free energy differences, Phys. Rev. Lett. 78 (14) (1997) 2690.
[54] M. De Koning, Optimizing the driving function for nonequilibrium free-energy calculations in the linear regime: A variational approach, J. Chem. Phys. 122 (10) (2005).
[55] V. Khanna, J. Anwar, D. Frenkel, M.F. Doherty, B. Peters, Free energies of crystals computed using Einstein crystal with fixed center of mass and differing spring constants, J. Chem. Phys. 154 (16) (2021).
[56] R. Freitas, M. Asta, M. De Koning, Nonequilibrium free-energy calculation of solids using LAMMPS, Comput. Mater. Sci. 112 (2016) 333–341.
[57] R. García Fernández, J.L. Abascal, C. Vega, The melting point of ice ih for common water models calculated from direct coexistence of the solid-liquid interface, J. Chem. Phys. 124 (14) (2006).
[58] W. Humphrey, A. Dalke, K. Schulten, VMD – visual molecular dynamics, J. Mol. Graph. 14 (1996) 33–38.
[59] J. Ahrens, B. Geveci, C. Law, C. Hansen, C. Johnson, 36-Paraview: An end-user tool for large-data visualization, Vis. Handb. 717 (2005) 1–50038.
[60] F. Mahmoudinobar, C.L. Dias, GRADE: A code to determine clathrate hydrate structures, Comput. Phys. Comm. 244 (2019) 385–391.
[61] R. Brunelli, Template Matching Techniques in Computer Vision: Theory and Practice, John Wiley & Sons, 2009.